Journal of Magnetism and Magnetic Materials 442 (2017) 25–35

Contents lists available at ScienceDirect

Journal of Magnetism and Magnetic Materials

journal homepage: www.elsevier.com/locate/jmmm

Research articles

Thermal and magnetic hysteresis associated with martensitic and magnetic phase transformations in $Ni_{52}Mn_{25}In_{16}Co_7$ Heusler alloy

A.S.B. Madiligama [a,*], P. Ari-Gur [b], Y. Ren [c], V.V. Koledov [d], E.T. Dilmieva [d], A.P. Kamantsev [d], A.V. Mashirov [d], V.G. Shavrov [d], L. Gonzalez-Legarreta [e], B.H. Grande [e]

[a] Department of Physics, Western Michigan University, Kalamazoo 49008-5252, USA
[b] Department of Mechanical and Aerospace Engineering, Western Michigan University, Kalamazoo 49008-5343, USA
[c] Argonne National Laboratory, 9700 S. Cass Ave, 433/D 008, 60439 Argonne, Illinois, USA
[d] Kotelnikov Institute of Radio-engineering and Electronics of RAS, Moscow 125009, Russia
[e] Department of Physics, University of Oviedo, Calvo Sotelo s/n, 33007 Oviedo, Spain

ARTICLE INFO

Article history:
Received 2 April 2017
Received in revised form 8 June 2017
Accepted 12 June 2017
Available online 15 June 2017

Keywords:
Giant magnetocaloric effect
Heusler alloys
Martensitic phase transformations
Magnetic phase transformations
Thermal hysteresis

ABSTRACT

Ni-Mn-In-Co Heusler alloys demonstrate promising magnetocaloric performance for use as refrigerants in magnetic cooling systems with the goal of replacing the lower efficiency, eco-adverse fluid-compression technology. The largest change in entropy occurs when the applied magnetic field causes a merged structural and magnetic transformation and the associated entropy changes of the two transformations works constructively. In this study, magnetic and crystalline phase transformations were each treated separately and the effects of the application of magnetic field on thermal hystereses associated with both structural and magnetic transformations of the $Ni_{52}Mn_{25}In_{16}Co_7$ were studied. From the analysis of synchrotron diffraction data and thermomagnetic measurements, it was revealed that the alloy undergoes both structural (from cubic austenite to a mixture of *7M* & *5M* modulated martensite) and magnetic (ferromagnetic to a low-magnetization phase) phase transformations. Thermal hysteresis is associated with both transformations, and the variation of the thermal hystereses of the magnetic and structural transformations with applied magnetic field is significantly different. Because of the differences between the hystereses loops of the two transformations, they merge only upon heating under a certain magnetic field.

Published by Elsevier B.V.

1. Introduction

The Magnetocaloric Effect (MCE) is a green technology with great potential to replace the eco-adverse, low- efficiency fluid compression cooling machines [1]. The Giant Magnetocaloric Effect (GMCE) is a very large entropy change associated with first-order phase transformation; it was first discovered in $Gd_5(Si_2Ge_2)$ [2]. Other ferromagnetic materials that demonstrate first-order phase transformations received attention as new magnetocaloric materials [3,4]. Starting in 2000, some *Ni-Mn-X* (*X = Ga, In, Sn, Sb*) Heusler alloys came into the spotlight as a room temperature magnetic refrigerant because their first-order martensitic phase transformations occurs around room temperature with a large entropy change [5–8]. When compared with other GMCE materials, these alloys are particularly attractive as magnetic refrigerants because they are inexpensive (no rare-earth elements), eco-friendly (no toxic elements), demonstrate good oxidation resistance, and have a high strength [1,9]. Additionally, the martensitic transformation temperature can be manipulated by substitution of *Co* in these alloys [1]. In some *Ni-Mn-In-Co* alloys, an applied magnetic field of sufficient strength, at a certain temperature range, will cause their highly-ordered martensitic phase to transform into a highly symmetric austenitic phase. The phase transformation temperature and strength of the required magnetic field depend on the composition of the alloy [10,11]. The main contributor to the large adiabatic cooling effect is the crystalline phase transformation. The magnetic entropy contribution from the spin alignment is relatively small but vital, as it is the driving force of the magneto-structural transformations [9].

The major drawback of both first-order martensitic and magnetic phase transformations is the thermal and magnetic hystereses associated with these transformations [12]. The irreversibility associated with magnetic and thermal hystereses reduces the coefficient of performance (COP) in each refrigeration cycle [3]. To optimize the working magnetic field of a magnetocaloric material, an

* Corresponding author.
E-mail address: amila.bandara@wmich.edu (A.S.B. Madiligama).

http://dx.doi.org/10.1016/j.jmmm.2017.06.080
0304-8853/Published by Elsevier B.V.

understanding of the behavior of thermal hysteresis of both martensitic and magnetic phase transformations as a function of the applied magnetic field is needed.

The current study was focused on the investigation of the thermal and magnetic hystereses associated with martensitic and magnetic phase transformations of the $Ni_{52}Mn_{25}In_{16}Co_7$ alloy. Therefore, two phase transformations, magnetic and crystalline, were treated separately to understand the behavior of thermal hysteresis associated with each transformation. The behavior of the thermal hysteresis associated with crystalline phase transformation was studied by analyzing the variation of martensitic and austenitic phase fractions with temperature and magnetic field. In the case of the magnetic phase transformations, ferromagnetic phase fraction was used to study the behavior of the associated thermal hysteresis.

2. Experimental description

Polycrystalline sample of the alloy was prepared by the arc-melting technique followed by annealing for 50 h at 1020 K. More details of sample preparation are described elsewhere [10]. The composition was determined using Rutherford Backscattering Spectrometry (RBS) measurements carried out at Western Michigan University's 6 MV Van de Graff accelerator laboratory. The projectile ion type (O^{+4}), the energy of the ion beam (15 MeV), and scattering angle (150°) were selected to obtain a maximum resolution between backscattered ions by *Ni* and *Co* atoms, which have similar atomic masses. The sample was prepared for the RBS measurements by polishing it using 5.0-μm aluminum-oxide powder as the abrasive. This process removed any oxidation present on the sample surface. RBS data were collected at two positions on the sample surface to confirm the homogeneity and improved statistics of the calculated composition. Table 1 summarizes the results of the RBS data analysis carried out using SIMNRA [13]. The average composition of the alloy was determined to be $Ni_{52}Mn_{25}In_{16}Co_7$. In-situ synchrotron diffraction measurements ($\lambda = 0.010804$ nm) were conducted on a polycrystalline sample (approximately $2 \times 2 \times 2\ mm^3$) at beamline 11-ID-C of the Advanced Photon Source at Argonne National Laboratory [14]. Even though powdered samples would have provided better diffraction patterns, the sample was kept intact to ensure that the alloy does not undergo any transformation during sample preparation. To improve the statistics of the diffraction pattern, the sample was rotated during data collection. Synchrotron data were collected as functions of both temperature and applied magnetic field. The four magnetic fields were 0, 2, 4, and 6 T. Under each magnetic field and under no applied magnetic field, data were recorded while heating and then cooling the sample in steps of 5 K. Also, diffraction measurements were performed at a constant temperature of 230 K while changing the magnetic field applied to the alloy from 0 to 6.5 T and back to 0 T in steps of 0.5 T. Rietveld refinements of the diffraction data were carried out using General Structure Analysis System (GSAS) [15] and GSAS EXPGUI [16]. To account for the apparent anisotropy in the polycrystalline sample, texture correction was performed during refinement. The refined crystalline structures were rendered using DRAWxtl software [17]. Thermomagnetic measurements of samples similar to those used for the synchrotron data were carried out: zero-field cooling (ZFC), field-cooling (FC), and field-heating (FH) routines, between 100 and 400 K, under four magnetic fields (0.005, 1, 2, and 3 T) using a Vibrating Sample Magnetometer (VSM). More details are available elsewhere [10].

3. Results and discussion

3.1. Crystalline structures and site occupancies

Diffraction patterns collected at 300 K under a 4 T magnetic field, and at 205 K without an applied magnetic field and compared with those calculated by the Rietveld method are shown in Fig. 1. At 300 K under 4 T applied magnetic field, the alloy is in the austenitic phase with cubic $L2_1$ structure. The schematic diagram of the refined cubic $L2_1$ structure and site occupancies of the constituent atoms are shown in Fig. 2-a. This structure belongs to the $Fm\bar{3}m$ space group. In the site-occupancy refinement of the austenitic phase, the composition of the alloy was constrained to the value determined by the RBS experiment. Additional constraints were used to avoid having too many parameters to refine what may lead to false refinement. Based on reported site occupancies of other *Ni-Mn* based Heusler alloys, cobalt atoms were allowed to occupy only regular *Ni-sites*. In our previous work on $Ni_{41}Mn_{39}In_{12}Co_8$ alloy, we found that all *Co* atoms occupy the regular *Ni-sites* [18]. Also, according to the formation energy calculations of the austenitic structure of *Ni-Mn-Ga* alloys, Bai et al. concluded that *Co* atoms preferentially occupy regular *Ni-sites* [19]. Because of the lower *In* concentration compared to the stoichiometric Ni_2MnIn alloy, *In* atoms were limited to their regular sites. It was found that the *In-sites* were occupied by ~65% of *In* and ~35% of *Mn*. Over 65% of the *Mn* atoms were found in their regular sites, with the rest of the regular *Mn-sites* are occupied by *Ni* atoms. *Ni* atoms were found in both regular *Ni*- (~86%) and *Mn*-sites (~35%). In diffusionless martensitic phase transformations, atoms keep their relative neighborhood unchanged and hence once the site occupancies of the austenitic phase were known, those in the martensitic phase could be determined by the relationship between the austenitic and martensitic crystalline structures.

Similar to the constraints used by Righi et al. [20,21], the following steps were taken to reduce the number of parameters in the refinements of the modulated martensitic structures: (1) the modulation occurs along the [0 0 1] crystallographic direction of the monoclinic unit cell (this corresponds to [1 1 0] direction in the austenitic structure); (2) only x- and y-coordinates of all atoms were allowed to refine, while the z-coordinate was kept constant; and (3) the amplitude of modulation of every atom in the (0 0 1) plane was the same. The observed and calculated diffraction patterns of the martensitic phase of the alloy (data were collected at 205 K without an applied magnetic field) are given in Fig. 1-*b*. There is a very good agreement between the observed and calculated diffraction profiles. The agreement confirms the validity of the assumptions made in assigning the site occupancies and constraints imposed in the refinements.

At 205 K under no applied magnetic field the alloy was found to be a mixture of two modulated monoclinic (*5M* and *7M*) structures. These modulated monoclinic structures belong to the *P 1 2/m 1*

Table 1
Summary of the RBS analysis.

Position	Energy of the O^{+4} ion beam (MeV)	Incident/scattering angle (°)	Calculated elemental composition (%)			
			Ni	Mn	In	Co
1	15	0/150	52.19 ± 0.40	24.89 ± 0.62	16.02 ± 0.23	6.96 ± 0.77
2	15	0/150	51.98 ± 0.37	25.07 ± 0.65	15.94 ± 0.26	7.00 ± 0.77

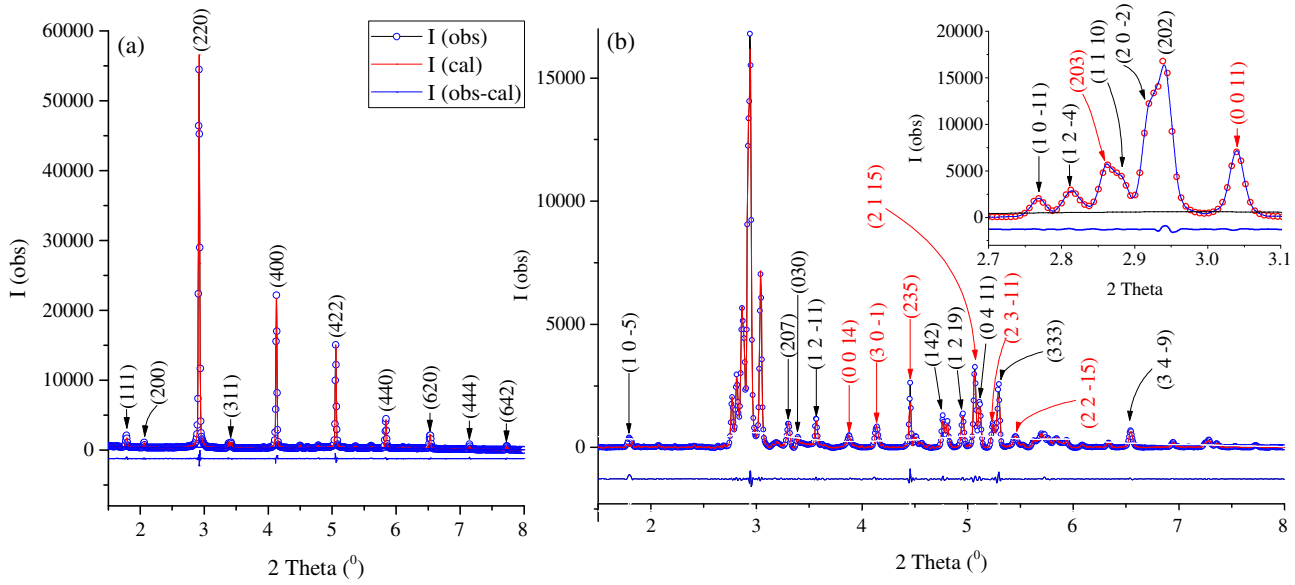

Fig. 1. Observed and calculated diffraction patterns in the austenitic and martensitic phases. (a) At 300 K and under 4 T magnetic field, the alloy was in the austenitic phase with cubic $L2_1$ crystalline structure ($Fm\bar{3}m$ space group). (b) At 205 K (0 T), the alloy is a mixture of two monoclinic structures with *7M* and *5M* modulations (*P 1 2/m 1* space group).

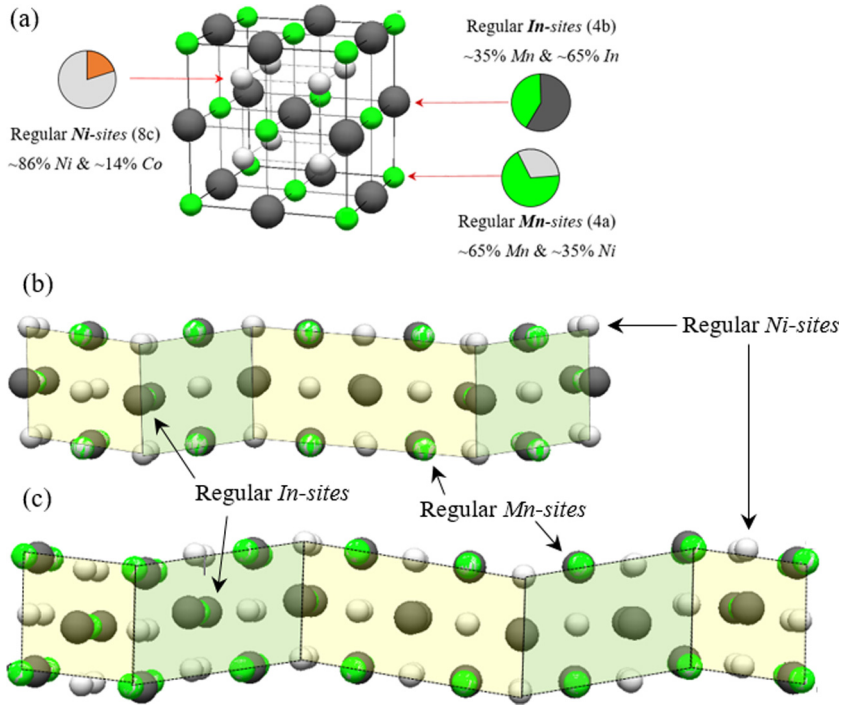

Fig. 2. Schematic diagrams of the crystalline structures of the $Ni_{52}Mn_{25}In_{16}Co_7$ alloy. (a) At 300 K (also, at 220 K under 6.5 T field) the alloy is in austenitic phase with $L2_1$ structure. The results of the site occupancy refinements are also given. At 220 K, under no applied magnetic field, the alloy is a mixture of *5M* (b) and *7M* (c) modulated martensite (*P 1 2/m 1*).

space group. The schematic diagrams of *5M* and *7M* modulated monoclinic structures are shown in Fig. 2-*b* and -*c*, respectively. Lattice parameters of all three crystalline structures, cubic, *5M* monoclinic and *7M* monoclinic, are given in Table 2 with the agreement factors of the final refinement cycle of each phase.

3.2. Magnetic field-induced martensitic phase transformations

External stimuli such as temperature, magnetic field, pressure, or stress may trigger martensitic phase transformations in some *Ni-Mn-X* based Heusler alloys [10,22]. To investigate the effect of

Table 2
Summary of the crystallographic information of the refined structures.

Crystalline structure	Space group	Lattice parameters ($\alpha = \gamma = 90°$)				Stacking sequence (Zhdanov notation)	Experimental conditions	Agreement factors		
		a (nm)	*b (nm)*	*c (nm)*	*β (°)*			R_w^b	R_p [c]	$\chi^{2\ d}$
Cubic $L2_1$	$Fm\bar{3}m$	5.994	5.994	5.994	90.00	–	300 K/4 T	6.71	4.69	4.86
5M monoclinic	*P 1 2/m 1*	4.501	5.758	22.406	89.12	$(2\bar{2}42\bar{2})$	205 K/0 T	4.08	3.66	3.58
7M monoclinic	*P 1 2/m 1*	4.272	5.479	28.518	91.38	$(2\bar{3}43\bar{2})$	205 K/0 T	4.08	3.66	3.58

[a]Agreement factors of the Rietveld refinements are defined as [15].

an applied magnetic field on the martensitic phase transformation of this alloy, diffraction data were collected under constant pressure (atmospheric pressure) and constant temperature (230 K) while increasing the applied magnetic field gradually from 0 to 6.5 T and back down to 0 T. The observed diffraction patterns under each magnetic field (in steps of 0.5 T) while increasing the field from 0 to 6.5 T, are shown in Fig. 3.

$$R_{WP}^{b} = 100\sqrt{\left(\sum_i w_i(I_0 - I_C)^2 / w_i I_0^2\right)}$$

$$R_P^c = 100\left(\sum |I_0 - I_C| / \sum I_0\right)$$

$$\chi^{2d} = \sum_i w_i(I_0 - I_C)^2 / (N_{obs} - N_{var})$$

where, I_0 and I_C: Observed and calculated diffraction intensities

w_i Weight assigned to each intensity

N_{obs} and N_{var}: The total number of observations and the number of variables in the least square refinement

χ^2: Goodness of the fit

From the observed diffraction patterns (Fig. 3), it is evident that the alloy is in the martensitic phase at 230 K under no applied magnetic field. Upon increasing the magnetic field, the alloy gradually transforms into austenite, and around 6 T the alloy completes its reverse martensitic phase transformation. To quantitatively study this magnetic field-induced martensitic phase transformation, the diffraction data were analyzed by Rietveld refinements to determine the phases and their fractions under each magnetic field. A convergence for the refinements of the martensitic phase was obtained for a mixture of *7M* and *5M* modulated monoclinic structures. Under 6.5 T, the alloy was in the austenitic phase with cubic $L2_1$ structure. This alloy had the same structure as the one found at 300 K under zero applied magnetic field. Rietveld refinements of the data collected under these different experimental conditions, at 230 K under 6.5 T and at 300 K under 0 T, are almost identical. For a complete study of the magnetic field induced martensitic phase transformation, the phase fractions of the austenitic and martensitic phases under different fields in steps of 0.5 T between 0 and 6.5 T were determined from the synchrotron diffraction data. The variation of the austenitic and martensitic phase fractions upon increasing and then decreasing applied magnetic field is shown in Fig. 4.

Fig. 4 demonstrates a complete reverse martensitic phase transformation from martensite to austenite upon increasing the field from zero to 6.5 T, and a complete forward martensitic phase transformation from austenite to martensite upon decreasing the field from 6.5 T to zero. Four characteristic magnetic fields were defined by following a procedure similar to that used to define the characteristic temperatures in a temperature-induced martensitic phase transformation. Four characteristic magnetic

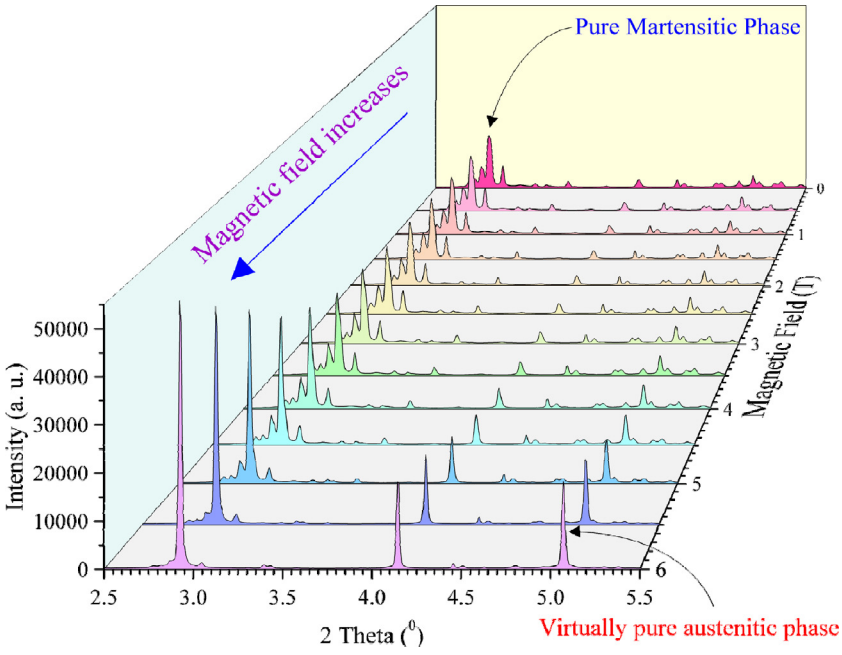

Fig. 3. The observed diffraction patterns fields, increasing magnetic fields increasing from 0 to 6.5 T in steps of 0.5 T. The experiment was carried out at constant temperature (230 K) and under atmospheric pressure. These diffraction patterns demonstrate the evolution of the austenitic phase from the martensitic phase upon gradually increased magnetic field.

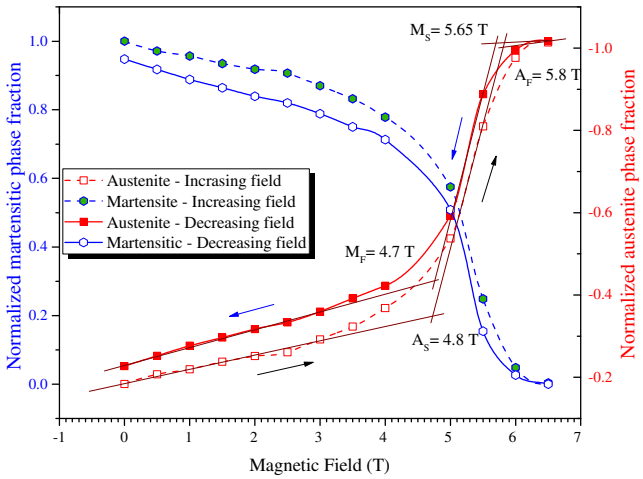

Fig. 4. Variation of the austenite and martensite phase fractions with applied magnetic field at 230 K while increasing the field from 0 to 6.5 T and then decreasing from 6.5 back to 0 T. Around the phase transformation, the magnetic hysteresis is about 0.2 T.

fields austenitic start (A_s^M), austenitic finish (A_F^M), martensitic start (M_s^M), and martensitic finish (M_F^M) – were determined by the intersections obtained by extrapolation of the linear parts of the austenitic phase-fraction versus magnetic field curves (Fig. 4). The magnetic hysteresis associated with the magnetic field induced martensitic phase transformation was determined by taking the average of $(A_s^M - M_F^M)$ and $(A_F^M - M_S^M)$.

Complete forward and reverse martensitic phase transformations of this alloy were observed upon changing the temperature from 300 K to 200 K and then from 200 K to 300 K, respectively. Fig. 5 compares the two reverse martensitic phase transformations: temperature-induced (closed circles) and magnetic-field-induced (open circles). Both temperature and applied magnetic field induce completely reversible martensitic phase transformations. Therefore, it can be concluded that the temperature and the magnetic field are equally capable of inducing martensitic

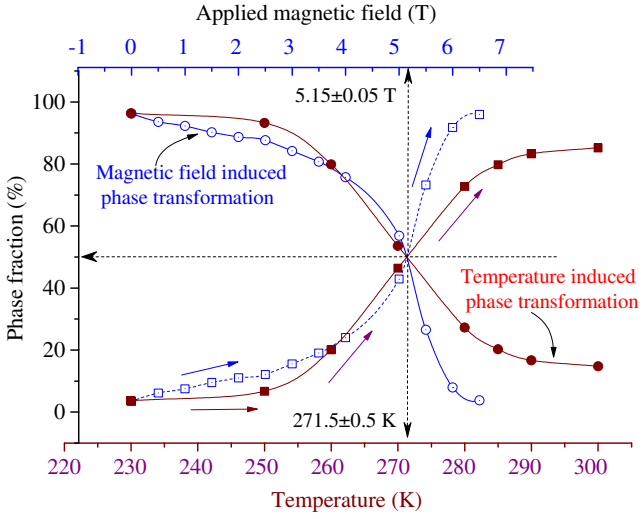

Fig. 5. Comparison of the variation of phase fractions of austenitic and martensitic phases with temperature in magnetic-field-induced (open symbols) and temperature-induced (closed symbols) martensitic phase transformation. In the case of magnetic field-induced transformation, data were collected at 230 K while changing the magnetic field from 0 to 6.5 T. In the temperature-induced phase transformation, data were collected while heating the alloy from 230 K to 300 K.

phase transformations in this alloy. Shamberger et al. have also demonstrated the temperature and magnetic field induced magnetic phase transformations in *Ni-Mn-Sn* alloys [23].

The starting conditions of both transformations were 230 K under no applied magnetic field. In the temperature-induced martensitic transformation around 271.5 K, the austenitic phase fraction grew to 50%. Alternatively, the same growth of the austenitic phase was achieved by increasing the magnetic field to 5.15 T. In the temperature-induced reverse martensitic phase transformation (Fig. 5), there is no significant change in the austenitic phase fraction until 250 K, then within the next 40 K, the alloy completes its martensitic transformation. Therefore, by choosing the correct starting temperature for the transformation, the magnetic-field-induced phase transformation can be made more effective (the alloy will complete its martensitic phase transformation under a lower magnetic field).

3.3. Phase fractions analysis

To investigate the characteristics of the martensitic phase transformation (such as transformation temperatures, thermal hysteresis associated with the phase transformations, and the effects of an applied magnetic field on the phase transformation temperature), phase fractions were calculated by the Rietveld refinements of the diffraction data collected under various experimental conditions. Phase fractions were determined by analyzing the synchrotron diffraction data collected under various experimental conditions. The results of the phase fraction analysis are summarized in Fig. 6. It shows the variation of the austenitic phase fraction while heating the alloy (from 200 to 300 K) under 4 magnetic fields (0, 2, 4, and 6 T) and then cooling (back to 200 K) under 3 magnetic fields; 2, 4, and 6 T.

Upon heating (under 0 T), the reverse-martensitic phase transformation starts at around 255 K. The alloy completes its reverse-martensitic phase transformation around 290 K. Under 2 T applied field the reverse martensitic phase transformation starts around 245 K and it finishes around 280 K. This implies a decreasing of the characteristic temperatures of the reverse-martensitic phase transformation when increasing the applied magnetic field. Similarly, a clear decrease of the austenitic start, A_S, and austenitic finish, A_F, was observed while increasing the magnetic field to 4 and 6 T.

Upon cooling under a 2 T applied magnetic field, forward-martensitic phase transformation starts at around 275 K. Under higher magnetic fields, 4 and 6 T, the forward phase transformation temperatures, M_S and M_F, decrease. That is, both forward- and reverse- phase transformation temperatures shift towards lower temperatures as the magnetic field applied to the alloy is increased. Similar behavior of phase transformation temperatures, shifting to lower temperatures with increasing magnetic field was reported in some other *Ni-Mn-In-Co* alloys [9].

As shown in Fig. 6, the austenitic phase fraction above the defined austenite-finish temperature A_F (*i.e.* above 290 K in all cases) is different under different magnetic fields. Under no applied magnetic field, the highest value of the austenitic phase fraction is about 85%, and that value increases to about 98% when the applied magnetic field is increased to 6 T (Fig. 6). With an increased magnetic field, an increasing number of martensitic variants transform into the austenitic phase. This trend is not limited to the austenitic phase. In the martensitic phase, (*i.e.* below the M_F), the austenitic phase fraction is higher under a higher magnetic field. All these observations confirm the effect of an applied magnetic field on the martensitic phase transformation of this alloy.

In order to investigate the martensitic phase transformation of the alloy in detail and quantitatively the normalized austenitic phase fraction was plotted against the temperature under all four

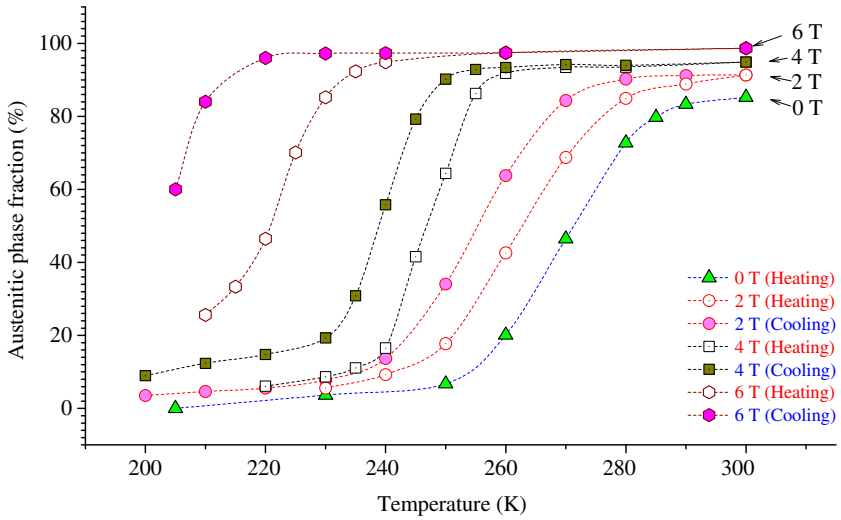

Fig. 6. Variation of the austenitic phase fractions between 200 and 300 K, under various experimental conditions. In the case of zero applied field to the alloy, data were collected only while heating the material. In all other cases, data were collected while heating from 200 K to 300 K (closed symbols) and then cooling back to 200 K (open symbols).

applied magnetic fields. The austenitic phase fraction was normalized with respect to the highest austenitic phase fraction under each magnetic field. Kinematic equations, (1) and (2), were used to fit the observed data points of the normalized austenitic phase fractions. These equations were adapted from the work of Li et al. [24]. The normalized austenitic phase fraction in the reverse-martensitic phase transformations (from twinned martensite to austenite phase) is given by Eq. (1). This equation was used to fit the data points in the reverse martensitic phase transformations under 0, 2, 4, and 6 T magnetic fields. The fitting parameters, T_0 and A_0, were refined by method of least squares, until there was good agreement between experimental data points and theoretical curve.

$$f_A = \frac{f_{M_0}}{1 + \exp\{\frac{(T_0 - T)}{A_0}\}} \quad (1)$$

where f_{M_0} is the initial martensitic phase fraction in the twinned-martensitic phase, which is taken as unity in all these cases, as the phase fractions were normalized with respect to the highest phase fraction value. T is the absolute temperature and T_0 is the phase transformation temperature (defined as the temperature at which the austenitic phase fraction is 50%). For the reverse phase transformations, $A_0 = (A_F - A_S)/Ce$ where C is a constant, determined empirically and e is the natural constant.

Eq. (2) gives the normalized austenitic phase fraction in the forward-martensitic phase transformations. This equation was used to fit the data points in the forward martensitic phase transformations under 2, 4, and 6 T magnetic fields. The fitting parameters, T_0 and M_0, were determined by following the same procedure as in the reverse martensitic phase transformations. In this equation $M_0 = (M_S - M_F)/Ce$.

$$f_A = \frac{1}{1 + \exp\{\frac{(T_0 - T)}{M_0}\}} \quad (2)$$

Fig. 7 shows the variation of the normalized austenitic phase fractions with temperature, while heating from the martensitic phase to the austenitic phase and cooling from the austenitic phase to the martensitic phase under those 4 different magnetic fields (0, 2, 4, and 6 T). The data-fitting curves, based on Eqs. (1) and (2),

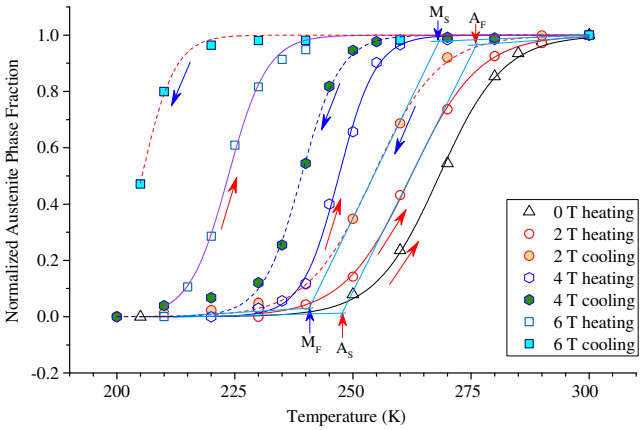

Fig. 7. Variation of normalized austenitic phase fraction (w.r.t. maximum austenitic phase fraction under each magnetic field) as a function of temperature while heating (open) and cooling (solid colors) under 4 different magnetic fields (0, 2, 4, and 6 T). Solid (heating) and dash (cooling) lines are the fit lines for the martensitic thermograms. Fit lines are based on Eqs. (1) and (2).

demonstrate good agreement with the experimental data. The refined values of the fitting parameters, A_0, M_0 and T_0, are summarized in Table 3.

The characteristic temperatures of the forward (M_S and M_F) and reverse (A_S and A_F) martensitic phase transformations were determined by the intersections, which were obtained by extrapolating the linear parts of the thermograms. Determination of the four characteristic temperatures in the case of 2 T magnetic field is shown in Fig. 7. All the characteristic temperatures of both forward- and reverse-phase transformations under all four magnetic fields are also given in Table 3.

The empirical constant C for each case was determined by substituting the appropriate characteristic phase transformation temperatures (M_S and M_F for the forward-phase transformation, and A_S and A_F for the reverse-phase transformation) and the appropriate fitting parameter A_0 or M_0 (Fig. 7). The value of C, determined for each phase transformation, is also summarized in Table 3. The mean value of the empirical constant C was found to be 1.48 ± 0.03. Eqs. (1) and (2), with the mean value of the empirical

Table 3
Least squares curve fitting parameters and characteristic temperatures of martensitic phase transformations of the studied alloy.

Trans. type	A_0 or M_0 (K)	T_0	A_S	A_F	M_S	M_F	C	Hysteresis (K)
0 T (h)	6.80 ± 0.33	268.26 ± 0.39	254.5 ± 0.5	281.0 ± 0.5	–	–	1.43 ± 0.05	–
2 T (h)	7.16 ± 0.17	261.32 ± 0.20	248.5 ± 0.5	276.5 ± 0.5	–	–	1.41 ± 0.03	7.04
2 T (c)	6.96 ± 0.21	254.28 ± 0.23	–	–	268.5 ± 0.5	240.5 ± 0.5	1.47 ± 0.04	
4 T (h)	3.93 ± 0.18	247.02 ± 0.20	239.0 ± 0.5	255.0 ± 0.5	–	–	1.49 ± 0.06	7.91
4 T (c)	4.14 ± 0.26	239.11 ± 0.26	–	–	247.5 ± 0.5	231.0 ± 0.5	1.46 ± 0.08	
6 T (h)	3.16 ± 0.37	224.40 ± 0.42	218.0 ± 0.5	231.0 ± 0.5	–	–	1.51 ± 0.13	19.04
6 T (c)	3.45 ± 0.30	205.36 ± 0.22	–	–	212.0 ± 0.5	198.5 ± 0.5	1.43 ± 0.10	

constant (1.48 ± 0.03) can be used to describe the behavior of both forward- and reverse-martensitic phase transformations. If the characteristic temperatures of the martensitic phase transformation are known, the variation of the normalized austenitic phase fraction with temperature can be fully described using those equations. These equations were used to construct the thermograms of both forward- and reverse-martensitic phase transformations under 1 and 3 T magnetic fields.

3.4. Thermomagnetic measurements

Fig. 8 displays the behavior of the mass magnetization as a function of temperature (in the range from 125 to 325 K) in FC (cooling), and FH (heating) routines under four applied magnetic fields (0.005, 1, 2, and 3 T). These thermomagnetic curves demonstrate a sharp increase in the magnetization around a certain temperature upon heating, and a sharp decrease in the magnetization upon cooling of the alloy. This indicates magnetic phase transformation from a low magnetization phase to a ferromagnetic phase upon heating and from a ferromagnetic to a low magnetization phase upon cooling. From Fig. 8, it is also evident that, the magnetic phase transformation temperatures decrease with increasing magnetic field. The weak magnetization in the martensitic phase is almost constant below a certain temperature (*e.g.* ~250 K without a magnetic field) in the martensitic phase.

Under 0.005 T magnetic field, the magnetization of the ferromagnetic austenitic phase increases at a very slow rate. This is because the 0.005 T magnetic field is not sufficient to saturate the ferromagnetic austenitic phase. However, in the case of higher magnetic fields (1–3 T), magnetization comes to a maximum value upon heating. This is where the alloy completes the reverse magnetic phase transformation. Above this temperature, the magnetization of the alloy gradually decreases with increasing temperature. This could be because upon heating the alloy in the austenitic phase, the ferromagnetic interactions decrease due to thermal agitation.

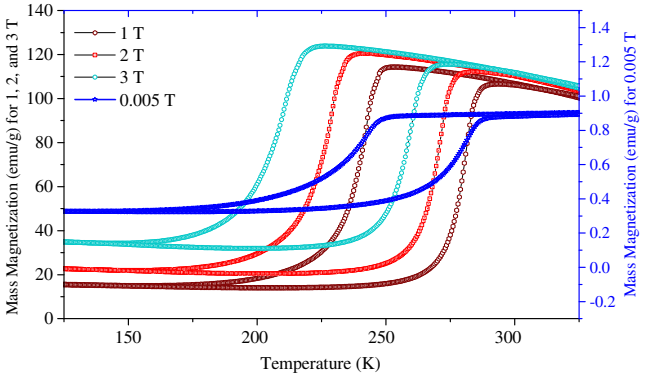

Fig. 8. Thermo-magnetization curves under different magnetic fields (.005, 1, 2, and 3 T). The vertical scale to the right side represents the mass magnetization under 0.005 T field and the one to the left side represents magnetization under higher magnetic fields (1, 2 and 3 T).

3.5. Magnetic phase transformations

From thermomagnetic measurements, it is evident that the alloy transforms from a ferromagnetic phase to a low-magnetization phase upon cooling. Magnetization versus temperature data can be transformed to ferromagnetic phase fraction versus temperature data by considering that the magnetization is directly proportional to the ferromagnetic phase fraction. The conversion procedure of the magnetization data to the ferromagnetic phase fraction used in this work is similar to the one described in Shamberger et al. [23]. Variation of the ferromagnetic phase fraction of the alloy with temperature, under four magnetic fields (0.005, 1, 2, and 3 T), is given in Fig. 9.

In order to study the characteristics of the magnetic phase transformations, magnetic phase transformation temperatures were defined as the intersections of extrapolations from the linear parts of the magnetic phase fraction versus temperature graph. The characteristic temperatures of the pure magnetic phase transformation - ferromagnetic start, FM_s, ferromagnetic finish, FM_F, lower magnetic state start, LM_s, and lower magnetic state finish, LM_F, under all three magnetic fields (1, 2, and 3 T) – are shown in Fig. 9. Additionally, two characteristic temperatures, $T_{1/2}C$ and $T_{1/2}H$, were defined. Similar to the characteristic temperature T_0 in the crystalline phase transformation, $T_{1/2}C$ and $T_{1/2}H$ are the temperatures at which the ferromagnetic phase fraction is 50%, while cooling and heating, respectively. All the characteristic transformation temperatures are listed in Table 4.

3.6. Magnetic field dependence of phase transformation temperatures

From the magnetic phase fraction analysis, it is evident that the magnetic phase transformation temperature is highly dependent upon the applied magnetic field to the alloy. All four characteristic temperatures of the magnetic phase transformation, FM_s, FM_F, LM_s, and LM_F, decrease with the increasing magnetic field, except at 0.005 T. Four characteristic temperatures under the 0.005 T field deviate from the rest. A small magnetic field (0.005 T in this study) is not sufficient to saturate the alloy magnetically, and hence a complete magnetic phase transformation will not occur [23]. On the other hand, under all other magnetic fields (1 T and higher), the alloy undergoes a complete phase transformation and the trend of the characteristic phase transformation temperatures is consistent.

The dependence of the martensitic transformation temperature on the applied magnetic field can be described qualitatively using the Clausius-Clapeyron equation [4,23,25,26]:

$$\frac{dT_0}{dH} = -\frac{\Delta M}{\Delta S} \tag{3}$$

where, $\Delta M = M^A - M^M$ is the difference between the magnetization of the two phases. Similarly, $\Delta S = S^A - S^M$ is the difference between

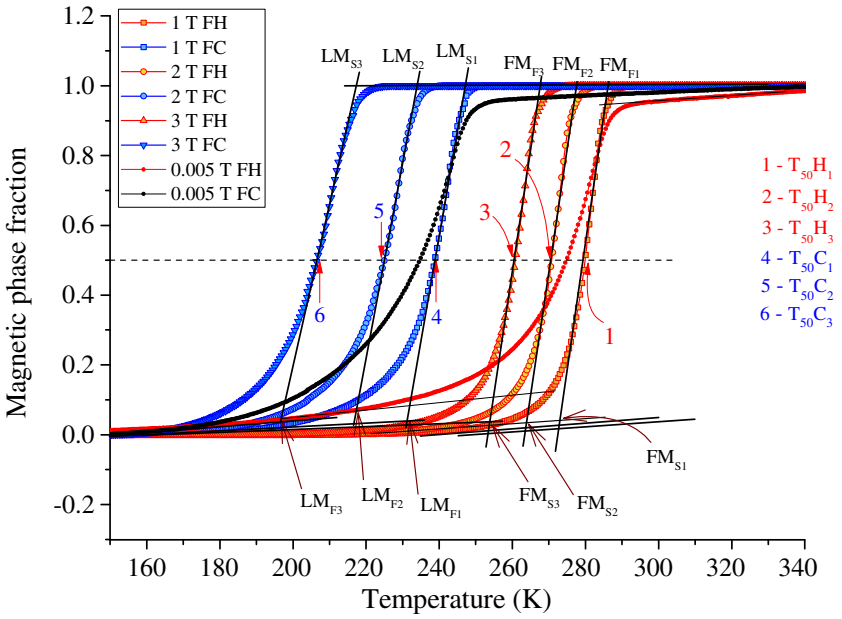

Fig. 9. Variation of the normalized ferromagnetic phase fraction with temperature. The characteristic temperatures of the magnetic phase transformations were determined from the intersections obtained by extrapolating the linear parts of the thermomagnetic curves.

Table 4
Characteristic temperatures of the pure magnetic phase transformation.

Magnetic field (T)	$T_{1/2}C$	$T_{1/2}H$	FM_s	FM_F	LM_s	LM_F	Hysteresis (K)
0.005	236.0 ± 0.5	275.0 ± 0.5	265.0 ± 0.5	287.0 ± 0.5	248.5 ± 0.5	224.0 ± 0.5	39.0 ± 0.7
1	239.5 ± 0.5	280.0 ± 0.5	275.0 ± 0.5	285.5 ± 0.5	246.5 ± 0.5	232.5 ± 0.5	40.5 ± 0.7
2	225.0 ± 0.5	271.0 ± 0.5	265.5 ± 0.5	276.5 ± 0.5	233.5 ± 0.5	217.0 ± 0.5	46.0 ± 0.7
3	206.5 ± 0.5	261.0 ± 0.5	255.5 ± 0.5	267.0 ± 0.5	217.5 ± 0.5	197.0 ± 0.5	54.5 ± 0.7

the entropies of the two phases and dT_0/dH is the rate of change of the transformation temperature with the applied field. Reverse phase transformation from low magnetization phase to ferromagnetic phase (i.e. $M^M \ll M^A$) results in a positive ΔM. The austenitic phase is cubic $L2_1$, which is more symmetric than the modulated monoclinic martensitic crystalline structures. Therefore, a positive entropy change results from a phase transformation from the martensitic phase(s) to the austenitic phase. Ito et al. [26] have investigated the entropy change ($\Delta S = S^A - S^M$) of a series of *Ni-Mn-In-Co* alloys. The calculated entropy change of all phase transformations of *Ni-Mn-In* and *Ni-Mn-In-Co* alloys from martensite to austenite phase upon heating are positive [26]. Upon applying a magnetic field, *Ni-Mn-In* alloys transform from a martensitic to austenitic phase causing a positive entropy change [27]. Therefore, with ΔM and ΔS both positive, the dT_0/dH is negative. Therefore, as the applied magnetic field increases, the phase transformation temperature further decreases.

Similar to the case of crystalline phase transformation, there is a thermal hysteresis associated with the magnetic phase transformation, which is highly dependent on the applied magnetic field. As the magnetic field increases, the thermal hysteresis associated with this magnetic phase transformation increases. The relationship between hysteresis and the applied magnetic field is not linear. The relationship between thermal hysteresis associated with magnetic phase transformation and applied magnetic field was obtained with a non-linear curve fitting to the calculated hysteresis data points. Eq. (4) gives the experimentally determined relationship between hysteresis and applied magnetic field and it can be approximated that the thermal hysteresis is proportional to the square of the applied magnetic field

$$\textit{Thermal hysteresis} = (1.499B^2 - 0.503B + 38.99)[K] \quad (4)$$

where B is given in Teslas.

3.7. Magnetostructural phase transformation

In order to study the coupled magneto-structural phase transformation, a variation of austenitic phase fraction with temperature during crystalline phase transformations under various magnetic fields was compared with the variation of the ferromagnetic phase fraction with temperature in pure magnetic phase transformations under the respective applied magnetic fields. Pure magnetic phase transformation data are available under four magnetic fields (0.005, 1, 2, and 3 T); The crystalline phase transformation data are available under 0, 2, 4, and 6 T applied magnetic fields. To compare the crystalline and magnetic phase transformations under 1 and 3 T fields, crystalline phase transformations were calculated for 1 and 3 T magnetic fields using the kinematic equations (Eqs. (1) and (2)) of the martensitic phase transformations.

Eq. (2) was used to generate the variation of austenitic phase fraction data in forward-phase transformations under 1 and 3 T magnetic fields, while the variation of the phase fraction of the austenitic phase in reverse transformation under 1 and 3 T magnetic fields was generated using Eq. (2). In order to use these equations, the parameters M_0 and T_0^M for forward phase transformations and the parameters A_0 and T_0^A for reverse phase transformations were determined. A trend of these parameters under 0, 2, 4, and 6 T magnetic fields was found by curve fitting of the experimental data. The respective parameters, M_0, A_0, T_0^M, and T_0^A for forward- and

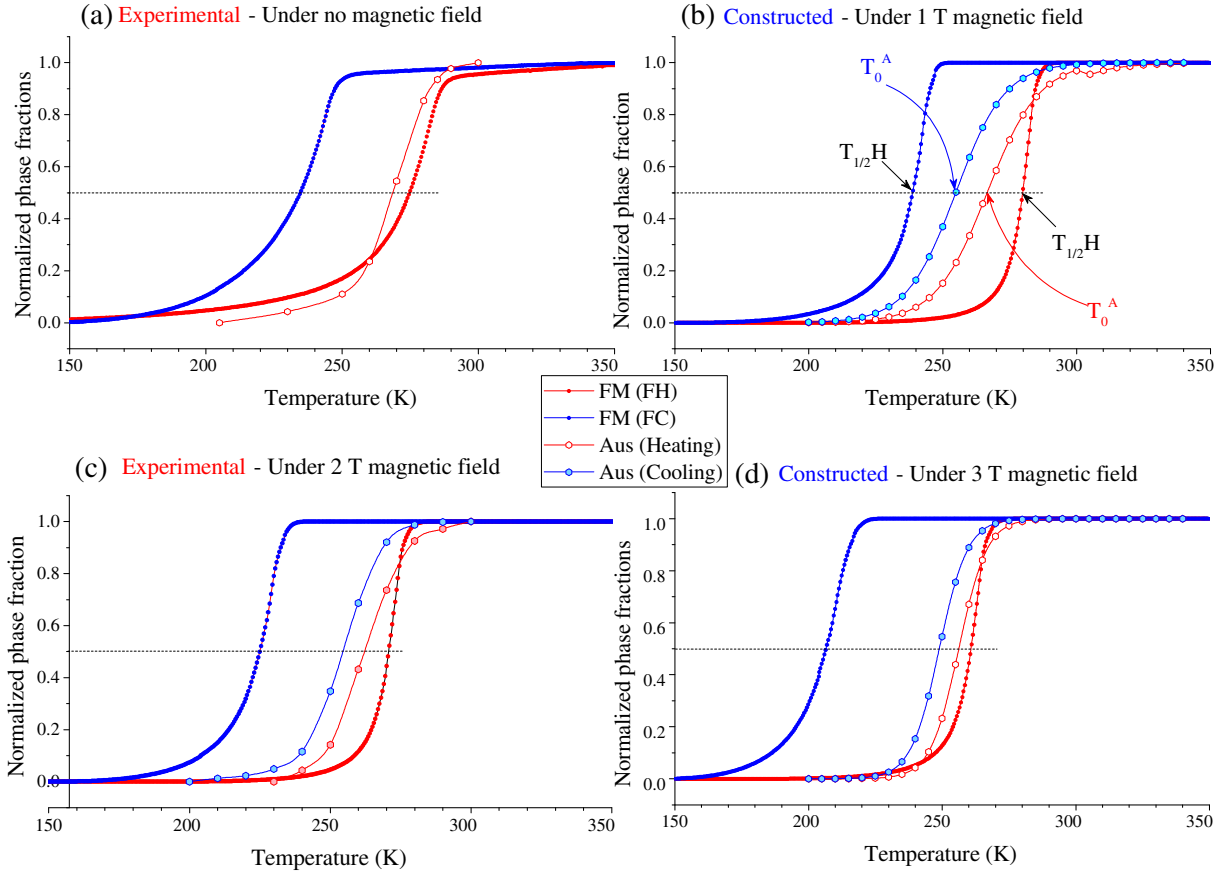

Fig. 10. Comparison of the thermal hysteresis and characteristic phase transformation temperatures of the crystalline and pure magnetic phase transformations. Variation of austenitic phase fraction and ferromagnetic phase fraction with temperature under (a) no applied magnetic field, (b) 1 T field, (c) 2 T, and (d) 3 T applied magnetic fields. In cases (b) and (c), normalized austenitic phase fraction data were constructed using kinematic Eqs. (1) and (2).

reverse-phase transformations under 1 and 3 T magnetic fields were then determined by interpolation.

With these parameters, two sets of data of the variation of the austenitic phase fraction with temperature under 1 and 3 T magnetic fields were constructed. The variation of the austenitic and the ferromagnetic phase fractions with temperature under the same magnetic fields were then compared, as shown in Fig. 10. This figure demonstrates the variation of austenitic and ferromagnetic phase fractions with temperature under four magnetic fields. In Fig. 10-*a* and -*c* (*i.e.* under ~0 and 2 T magnetic fields, respectively), both austenitic and ferromagnetic phase fraction data were determined experimentally. However, under 1 and 3 T the values of phase fraction of the austenitic phase were determined using the kinematic Eqs. (1) and (2) (Fig. 10-*b* and -*d*).

From Fig. 10 it is evident that the thermograms of the first-order crystalline phase transformation and magnetic phase transformation do not follow the same path. Under all studied magnetic fields, the thermal hysteresis loops of the crystalline phase transformations are narrower than those for the magnetic phase transformations. Also, the thermograms of the reverse-phase transformations (both crystalline and magnetic) are closer to each other when compared with the thermograms of the forward-phase transformations. The crystalline and pure magnetic phase transformation temperatures were compared by taking the differences between T_0^M - $T_{1/2}C$ (for forward-phase transformations) and between T_0^A - $T_{1/2}H$ (for reverse-phase transformations). The calculated values (Table 5) also confirm that the characteristic temperatures of the reverse phase transformations are closer to each other than that of the forward-phase transformations.

In the applied field range (0.005–3 T), the difference between T_0^A and $T_{1/2}H$ reaches a maximum at 1 T; it then gradually decreases with further increase in magnetic field. Under 3 T, the difference between T_0^A and $T_{1/2}H$ is only 4.0 K, which is still larger than the

Table 5
Phase transformation temperatures and hysteresis associated with crystalline and magnetic phase transformations.

Field (T)	Reverse phase transformation (Heating)		Forward phase transformation (Cooling)		Thermal hysteresis (K)		Temperature difference between phase transformations (K)	
	T_0^A (K)	$T_{1/2}H$ (K)	T_0^M (K)	$T_{1/2}C$ (K)	Crystalline	Magnetic	Reverse	Forward
0	268.5 ± 0.5	275.0 ± 0.5	–	234.5 ± 0.5	–	40.5 ± 0.7	6.5 ± 0.7	–
1	266.5 ± 0.5	280.0 ± 0.5	255.5 ± 0.5	239.0 ± 0.5	11.0 ± 0.5	40.5 ± 0.7	13.5 ± 0.7	−16.5 ± 0.7
2	262.0 ± 0.5	271.0 ± 0.5	255.0 ± 0.5	225.0 ± 0.5	7.0 ± 0.5	46.0 ± 0.7	9.0 ± 0.7	−30.0 ± 0.7
3	256.5 ± 0.5	260.5 ± 0.5	249.0 ± 0.5	206.0 ± 0.5	7.5 ± 0.5	54.5 ± 0.7	4.0 ± 0.7	−43.0 ± 0.7

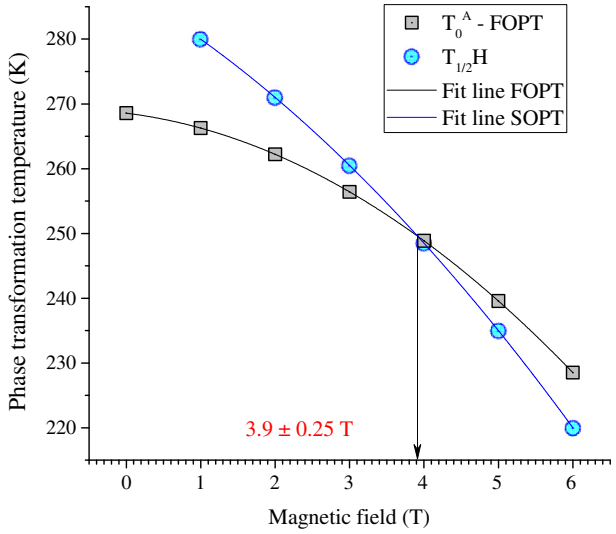

Fig. 11. Variation of the phase transformation temperature, in both crystalline (squares) and magnetic (circles) phase transformations, with the applied magnetic field.

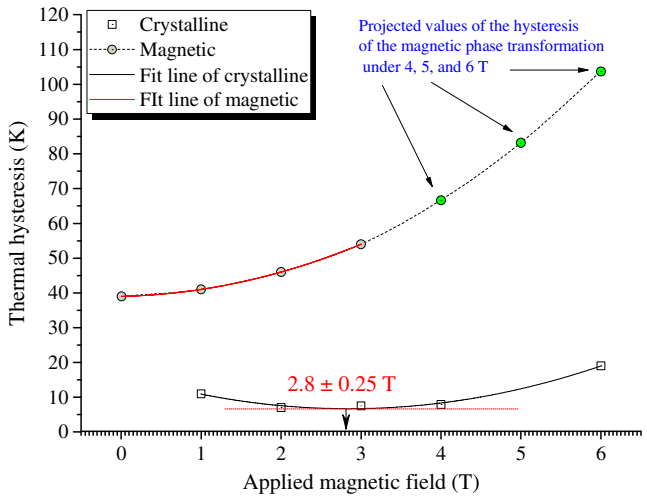

Fig. 12. Behavior of the thermal hysteresis associated with first-order crystalline phase transformation (squares) and magnetic phase transformation (circles) with applied magnetic field.

value under no magnetic field. Therefore, it can be anticipated that a merged magneto-structural reverse phase transformation (*i.e.* upon heating of the alloy) will occur under a magnetic field which is greater than 3 T. For magnetic fields which are 1 T and higher, T_0^A and $T_{1/2}H$ is inversely proportional to the applied magnetic field. In order to determine the temperature at which a merged magneto-structural reverse-phase transformation is possible, phase transformation temperatures, T_0^A and $T_{1/2}H$, were plotted against the applied magnetic field (Fig. 11).

Fig. 11 represents the variation of phase transformation temperatures of the reverse phase transformations, magnetic (circles) and crystalline (squares), with the applied magnetic field to the alloy. Magnetic phase transformation temperatures under higher magnetic fields (4, 5, and 6 T) were determined by extrapolation. Both magnetic and crystalline reverse-phase transformation temperatures decrease with the applied magnetic field. However, the rate of decrease of the phase transformation temperature with an increased magnetic field is not the same. Therefore, two curves intersect at ~3.9 T, and under that magnetic field a merged magnetostructural phase transformation is anticipated.

For magnetic fields greater than 1 T, the difference between T_0^M and $T_{1/2}C$ (*i.e.* the difference between the forward phase transformation temperatures) is directly proportional to the applied magnetic field. Therefore, the forward phase transformations (magnetic and structural) do not merge under any magnetic field because of the large difference between their thermal hysteresis.

3.8. Thermal hystereses associated with magnetic and crystalline phase transformations

The thermal hysteresis associated with crystallographic and magnetic phase transformations under each magnetic field was calculated by taking the difference between T_0^M and T_0^A and between $T_{1/2}H$ and $T_{1/2}C$, respectively (a summary of these calculations is given in Table 5). The thermal hystereses versus applied magnetic fields were plotted and the trendline of the data points are illustrated in Fig. 12. The thermal hystereses under 4, 5, and 6 T magnetic fields were found by extrapolation of the trendline of thermal hysteresis versus the applied magnetic field graph.

From Fig. 12, the thermal hysteresis of the magnetic phase transformation (MPT) increases monotonically with the magnetic field under which the phase transformation takes place. While, the thermal hysteresis of the first-order phase transformation (FOPT) has a minimum at a field of 2.8 ± 0.25 T. The thermal hysteresis associated with MPT is much higher than that of the FOPT. Thermal hystereses are intrinsic to the first-order phase transformations. As a result, in *Ni-Mn-X* based alloys, even though a large reversible entropy change is observed, only a fraction of the material transform cyclically between the martensitic and the austenitic phases upon application and removal of a magnetic field. Consequently, hysteresis associated with first-order phase transformations diminishes the maximum achievable coefficient of performance in a refrigeration cycle, based on the giant magnetocaloric effect [28–30].

Even though the observed magnetic entropy change increases with the increasing of the magnetic field under which the phase transformation takes place, it is crucial to take the associated thermal hysteresis losses into account. Therefore, the optimum value of the maximum magnetic field could be calculated by considering a maximum entropy change of the first order phase transformation and minimum thermal hysteresis loss associated with it.

4. Conclusions

In this study, magnetic and crystalline phase transformations of the $Ni_{52}Mn_{25}In_{16}Co_7$ Heusler alloy were each treated individually. The alloy undergoes both magnetic phase transformations from ferromagnetic to a phase with low magnetization and structural phase transformation from $L2_1$ cubic to a mixture of *5M* and *7M* modulated martensitic phases. Both changes, of temperature from 200 to 300 K (under no magnetic field), and magnetic field from 0 to 6.5 T (at 230 K), cause a complete reversible martensitic phase transformation in this alloy. There are also associated thermal hystereses for both magnetic and crystalline phase transformations. In the studied range, the hysteresis associated with the magnetic phase transformation is about four times larger than that of the crystalline phase transformation. The thermal hysteresis associated with a magnetic phase transformation increases with an increased magnetic field. The thermal hysteresis is approximately proportional to the square of the applied magnetic field. The thermal hysteresis associated with the first-order phase transformation has a minimum approximately under a 2.8 T magnetic field.

Characteristic temperatures of both crystalline and magnetic phase transformations decrease with an increasing magnetic field, but at a different rate. Thus, the difference between the equilibrium temperatures of the crystalline and magnetic phase transformation (upon heating) decreases with an increased magnetic field, and a merged magneto-structural phase transformation can be anticipated around 3.9 T (250 K). Because of the large difference in the hystereses, the crystalline and magnetic phase transformations upon cooling do not merge under any magnetic field. The nature of the observed phenomena deserves deeper investigation; for example, comparative study of the crystal and magnetic structures using AFM and MFM microscopy or by Scanning Electron Microscopy with Polarization Analysis (SEMPA).

Acknowledgement

This study was supported by award No. RUP1-7028-MO-11 from the US Civilian Research and Development Foundation (CRDF Global) and by the National Science Foundation under Cooperative Agreement No. OISE-9531011. The study was also supported by the Russian Science Foundation Grant No. 14-22-00279. The authors wish to also acknowledge the US National Science Foundation award number NSF-0831951. Advance photon source use was supported by the US Department of Energy, Office of Science, under Contract No. DE-AC02-06CH11357. Last but not least, the authors wish to acknowledge Dr. A. Kayani of the Department of Physics at Western Michigan University for his help in the Rutherford backscattering experiment.

References

[1] A. Kitanovski, U. Plaznik, U. Tomc, A. Poredos, Int. J. Refrig. 57 (2015) 288–298.
[2] V.K. Pecharsky, J.K.A. Gschneidner, Phys. Rev. Lett. 78 (1997) 4494.
[3] A. Giguere, M. Foldeaki, B. Ravi Gopal, R. Chahine, T.K. Bose, A. Frydman, J.A. Barclay, Phys. Rev. Lett. 83 (1999) 2262.
[4] A. Planes, L. Manosa, M. Acet, J. Phys.: Condens. Matter 21 (2009) 233201.
[5] V.V. Khovaylo, K.P. Skokov, Y.S. Koshkid'ko, V.V. Koledov, V.G. Shavrov, V.D. Buchelnikov, S.V. Taskaev, H. Miki, T. Taskaev, A.N. Vasiliev, Phys. Rev. B: Condens. Matter 78 (2008) 060403.
[6] P.A. Bhobe, K.R. Priolkar, A.K. Nigam, Appl. Phys. Lett. 91 (2007) 242503.
[7] J. Du, Q. Zheng, W.J. Ren, W.J. Feng, X.G. Liu, Z.D. Zhang, J. Phys. D: Appl. Phys. 40 (2007) 5523.
[8] M. Khan, N. Ali, S. Stadler, J. Appl. Phys. 101 (2007) 053919.
[9] J. Liu, T. Gottschall, K.P. Skokov, J.D. Moore, O. Gutfleisch, Nat. Mater. 11 (2012) 620.
[10] A. Kamantsev, V. Koledov, E. Dilmieva, A. Mashirov, V. Shavrov, J. Cwik, I. Tereshina, V. Khovaylo, M. Lyange, L. Gonzalez-Legarreta, B. Hernando, P. Ari-Gur, EPJ Web Conf. 75 (2014) 04008.
[11] A.P. Kamantsev, V.V. Koledov, A.V. Mashirov, E.T. Dilmieva, V.G. Shavrov, J. Cwik, I.S. Tereshina, Bull. Russ. Acad. Sci. Phys. 78 (2014) 936.
[12] V. Basso, C.P. Sasso, K.P. Skokov, O. Gutfleisch, V.V. Khovaylo, Phys. Rev. B: Condens. Matter 85 (2012) 014430.
[13] M. Mayer, SIMNRA User's Guide, Technical Report IPP 9/113, Max-Planck-Institut Fur Plasmaphysik, Garching, Germany, 1997.
[14] Advanced Photon Source [Online], Available from: <http://www.aps.anl.gov/Beamlines/Directory/>.
[15] A. Larson, R. Von Dreele, General structure analysis system (GSAS), Los Alamos Nat. Lab. Rep. LAUR 86–748 (2004).
[16] B.H. Toby, EXPGUI, a graphical user interface for GSAS, J. Appl. Cryst. 34 (2001) 210.
[17] L.W. Finger, M. Kroeker, B.H. Toby, DRAWxtl, an open-source computer program to produce crystal-structure drawings, J. Appl. Cryst. 40 (2007) 188.
[18] A.S.B. Madiligama, P. Ari-Gur, V.G. Shavrov, V.V. Koledov, S. Calder, A.V. Mashirov, A.P. Kamantsev, E.T. Dilmieva, L. Gonzalez-Legarreta, B.H. Grande, V. V. Vega, A. Kayani, Smart Mater. Struct. 25 (2016) 085013.
[19] J. Bai, J.M. Raulot, Y. Zhang, C. Esling, X. Zhao, L. Zuo, Appl. Phys. Lett. 98 (2011) 164103.
[20] L. Righi, F. Albertini, E. Villa, A. Paoluzi, G. Calestani, V. Chernenko, S. Besseghini, C. Ritter, F. Passaretti, Acta Mater. 56 (2008) 4529.
[21] L. Righi, F. Albertini, S. Fabbrici, A. Paoluzi, Mater. Sci. Forum 684 (2011) 105.
[22] R. Kainuma, Y. Imano, W. Ito, Y. Sutou, H. Morito, S. Okamoto, O. Kitakami, K. Oikawa, A. Fujita, T. Kanomata, K. Ishida, Nature 439 (2006) 957–960.
[23] P.J. Shamberger, F.S. Ohuchi, Phys. Rev. B 79 (2009) 144407.
[24] L. Li, Q. Li, F. Zhang, InTech 215–260 (2013).
[25] J. Kim, F. Inaba, T. Fukuda, T. Kakeshita, Acta Mater. 54 (2005) 493.
[26] W. Ito, Y. Imano, R. Kainuma, Y. Sutou, K. Oikawa, K. Ishida, Metall. Mater. Trans. A 38 (2007) 759–766.
[27] T. Krenke, E. Duman, M. Acet, E.F. Wassermann, X. Moya, L. Mañosa, A. Planes, Nat. Mater. 4 (2005) 450.
[28] V. Provenzano, A.J. Shapiro, R.D. Shull, Letters to nature, 429 (2004) 853.
[29] V.K. Sharma, M.K. Chattopadhyay, S.B. Roy, J. Phys. D: Appl. Phys. 40 (2007) 1869–1873.
[30] E.T. Dilmieva, A.P. Kamantsev, V.V. Koledov, A.V. Mashirov, V.G. Shavrov, J. Cwik, I.S. Tereshina, Phys. Solid State 58 (1) (2016) 81.